HHS Public Access

Author manuscript

Acta Biomater. Author manuscript; available in PMC 2021 September 01.

Published in final edited form as:

Acta Biomater. 2020 September 01; 113: 217–227. doi:10.1016/j.actbio.2020.06.015.

Spatially-directed cell migration in acoustically-responsive scaffolds through the controlled delivery of basic fibroblast growth factor

Xiaofang Lu[1], **Hai Jin**[1,2], **Carole Quesada**[1], **Easton C. Farrell**[1], **Leidan Huang**[1,3], **Mitra Aliabouzar**[1], **Oliver D. Kripfgans**[1,4,5], **J. Brian Fowlkes**[1,4,5], **Renny T. Franceschi**[5,6], **Andrew J. Putnam**[5], **Mario L. Fabiilli**[1,4,5]

[1]Department of Radiology, University of Michigan, Ann Arbor, MI, USA

[2]School of Medicine, Second Affiliated Hospital of South China University of Technology, Guangzhou, China

[3]Department of Ultrasound, Second Affiliated Hospital of Army Medical University, Chongqing, China

[4]Applied Physics Program, University of Michigan, Ann Arbor, MI, USA

[5]Department of Biomedical Engineering, University of Michigan, Ann Arbor, MI, USA

[6]Dental School, University of Michigan, Ann Arbor, MI, USA

Abstract

Hydrogels are commonly used in regenerative medicine for the delivery of growth factors (GFs). The spatial and temporal presentations of GFs are critical for directing regenerative processes, yet conventional hydrogels do not enable such control. We have developed a composite hydrogel, termed an acoustically-responsive scaffold (ARS) where release of a GF is non-invasively and spatiotemporally-controlled using focused ultrasound. The ARS consists of a fibrin matrix doped with a GF-loaded, phase-shift emulsion. The GF is released when the ARS is exposed to suprathreshold ultrasound via a mechanism termed acoustic droplet vaporization. In this study, we investigate how different spatial patterns of suprathreshold ultrasound can impact the biological response upon *in vivo* implantation of an ARS containing basic fibroblast growth factor (bFGF). ARSs were fabricated with either perfluorohexane (bFGF-C6-ARS) or perflurooctane (bFGF-C8-ARS) within the phase-shift emulsion. Ultrasound generated stable bubbles in bFGF-C6-ARS, which inhibited matrix compaction, whereas transiently stable bubbles were generated in bFGF-C8-ARS, which decreased in height by 44% within one day of implantation. The rate of bFGF

Corresponding Author: Mario Fabiilli, Ph.D., University of Michigan, 3226A Medical Sciences Building I, 1301 Catherine Street, Ann Arbor, MI 48109-5667, Phone: 734-647-9326, mfabiill@umich.edu.

Declaration of interests

The authors declare that they have no known competing financial interests or personal relationships that could have appeared to influence the work reported in this paper.

release and distance of host cell migration were up to 6.8-fold and 8.1-fold greater, respectively, in bFGF-C8-ARS versus bFGF-C6-ARS. Ultrasound increased the formation of macropores within the fibrin matrix of bFGF-C8-ARS by 2.7-fold. These results demonstrate that spatially patterning suprathreshold ultrasound within bFGF-C8-ARS can be used to elicit a spatially-directed response from the host. Overall, these findings can be used in developing strategies to spatially pattern regenerative processes.

Graphical Abstract

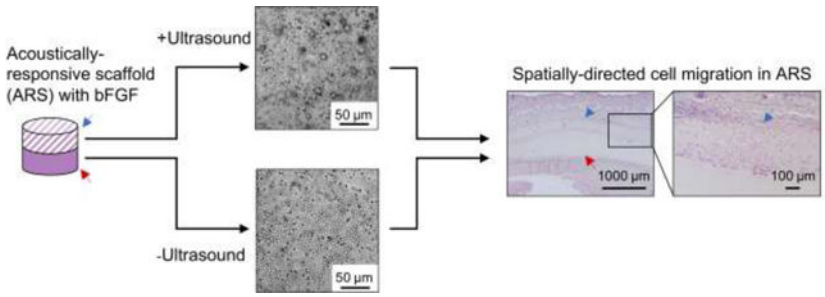

Keywords

ultrasound; drug delivery; fibrin; acoustic droplet vaporization; phase-shift emulsion; migration; basic fibroblast growth factor

Introduction

Hydrogels are widely used within the field of regenerative medicine for the delivery of cells, cytokines, and/or genetic material. As a surrogate for the native extracellular matrix, a hydrogel consists of a cross-linked polymer network with a high water content. Cytokines, such as growth factors (GFs), can be incorporated directly within the hydrogel during polymerization, thus typically yielding a delivery system that exhibits a burst release due to the low affinity of the GF to the hydrogel [1]. To extend the release kinetics, which is often more desirable in regenerative medicine applications, two approaches are generally utilized. First, the affinity of the GF for the hydrogel is increased (e.g., via the addition of binding motifs to the GF and/or hydrogel) [2]. Second, the GF is formulated within particles with defined release kinetics, and a composite hydrogel is formed via the addition of GF-loaded particles to the hydrogel [3]. Thus, based on these strategies, it becomes evident that honing the temporal release of GFs is critical for regenerative applications in an effort to recapitulate endogenous signaling.

In addition to temporal selectivity, the spatial control of GF delivery is also important. Yet, hydrogels are inherently isotropic on the size order relevant for GF diffusion, and thus strategies are employed to impart anisotropy. For example, microfluidic devices can produce spatial gradients of GFs within hydrogels, as has been done using patterned microchannels in a methacrylated dextran gel [4]. However, the utility of this approach for *in vivo* studies is limited. Strategies more amenable to *in vivo* studies include the development of bi-layer scaffolds, for example poly(lactide-co-glycolide) scaffolds with vascular endothelial growth

factor (VEGF) and platelet derived growth factor (PDGF) in separate layers [5]. Photopatterning the crosslinking of hydrogels with ultraviolet light can also produce tight spatial patterns of biomolecules, as demonstrated in norborene-functionalized hyaluronic acid hydrogels with signaling peptides [6] or dual-crosslinked heparin/alginate hydrogels with VEGF [7]. Patterning of GFs can also be achieved using 3D printing, as seen with VEGF in biphasic scaffolds containing alginate and calcium phosphate cement [8]. Despite the tight spatial selectivity imparted by the aforementioned approaches, these techniques rely on *priori* design of the scaffold. Thus, once the scaffold is implanted *in vivo*, the spatial and temporal kinetics of release typically cannot be altered. The ability to spatiotemporally modulate release kinetics of GFs post-implantation via external actuation would be beneficial in directing tissue regeneration.

We have developed a composite hydrogel where release of GFs is non-invasively and spatiotemporally-controlled using focused ultrasound (US). The mechanism for release is acoustic droplet vaporization (ADV), whereby phase-shift emulsions are vaporized into bubbles when exposed to suprathreshold US (i.e., acoustic pressures above the threshold for ADV)[9]. The phase-shift emulsion is embedded into a fibrin hydrogel to yield an acoustically-responsive scaffold (ARS)[10, 11]. GFs are incorporated into the ARS by formulating a phase-shift emulsion as a double emulsion with a water-in-perflurocarbon (PFC)-in-water structure (W_1/PFC/W_2). The GF payload is contained within the W_1 phase and is released when the PFC is vaporized during ADV, thus disrupting the morphology of the double emulsion. ADV is initiated by superharmonic focusing of the rarefactional component of the US wave, thereby generating a vapor nucleus within the PFC phase [12, 13]. The vaporization of the PFC phase is mechanical and thus pulsed US can be used to trigger ADV, hence minimizing any thermal bioeffects related to the US exposure. We have demonstrated that ADV can be generated in hydrogel phantoms using a clinical, therapeutic US system [14].

In prior publications, we studied how ARSs can be used for the controlled release of basic fibroblast growth factor (bFGF), which displays broad mitogenic activity on mesoderm-derived cells. For example, bFGF induces endothelial cell migration [15], tubule formation [16], and proliferation of fibroblasts [17]. ADV-triggered delivery of bFGF from ARSs was shown to stimulate endothelial network formation [18]. In subcutaneously implanted ARSs, release of bFGF via ADV was shown to increase microvessel density and perfusion [19]. Additionally, ARSs can be constructed to enable sequential delivery of payloads, as demonstrated in studies using two fluorescent dextrans [20] as well as bFGF and PDGF [21].

In this study, we investigate how spatial patterns of ADV and bFGF release within an ARS can elicit a spatially-directed, biological response (i.e., host cell migration) upon *in vivo* implantation. Cells migrate in response to biochemical and biophysical signals in their local microenvironment, including cues provided by neighboring cells. Cell migration is critical during homeostatic and pathological processes such as angiogenesis [22], immune response [23], and fibrous tissue repair [24]. Directed cell migration has been achieved by immobilizing spatial gradients of GFs [25, 26]. As will be shown in this study, spatially patterning suprathreshold US within ARSs can be used to elicit a spatially patterned

response from the host. Previously, spatially-defined patterns of ADV have been used to impact acoustic fields [27], enhance thermal therapy [14], and control chemical reactions [28]. Here, monodispersed phase-shift emulsions with bFGF were generated with two different species of PFC. *In vitro* studies investigated bFGF release and ARS morphology. For *in vivo* studies, ARSs were exposed to different spatial patterns of suprathreshold US. *In situ* ARS morphology was longitudinally monitored using B-mode US. Using histology and immunohistochemistry, explanted ARSs and surrounding tissues were morphometrically analyzed for scaffold compaction, macroporosity, host cell migration, granulation layer thickness, and vascularization.

1. Materials and Methods

2.1 Preparation and characterization of phase-shift emulsion

Phase-shift double emulsions with a W_1/PFC/W_2 structure were prepared by modifying a previously described method [19]. Briefly, a triblock fluorosurfactant, consisting of Krytox 157FSH (CAS# 51798-33-5, DuPont, Wilmington, DE, USA) and polyethylene glycol (MW: 1000, CAS#: 24991-53-5, Alfa Aesar, Ward Hill, MA USA), was dissolved at 2% (w/w) in perfluorohexane (C6, CAS#: 355-42-0, Strem Chemicals, Newburyport, MA USA) or perfluorooctane (C8, CAS#: 307-34-6, Alfa Aesar, MA USA). The PFC phase was combined at 2:1 (v/v) with a W_1 phase containing 1 mg/mL recombinant human basic fibroblast growth factor (bFGF, Cat#: GF003AF, EMD Millipore, Temecula, CA USA), 10 mg/mL bovine serum albumin (Sigma-Aldrich, St. Louis, MO USA), and 7.5 μg/mL heparin (Cat #: 375095, Calbiochem, San Diego, CA, USA) in phosphate-buffered saline (PBS, Life Technologies, Grand Island, NY USA). The phases were sonicated (Q55 with CL-188 immersion probe, QSonica, Newton, CT, USA) for 30 sec while on ice. For blank emulsions, the W_1 phase contained only PBS.

The resulting primary emulsion and W_2 phase, consisting of 50 mg/mL Pluronic F68 (CAS# 9003-11-6, Sigma-Aldrich) in PBS, were pumped at 1 μL/min and 10 μL/min, respectively, into a quartz microfluidic chip (Cat#: 3200146, junction: 14 × 17 μm, hydrophilic coating, Dolomite, Royston, United Kingdom). The resulting double emulsion was characterized using a Coulter counter (Multisizer 4, Beckman Coulter, Brea, CA USA) with a 50 μm aperture. In this work, each ARS group is designated by the payload and PFC within the emulsion (e.g., bFGF-C6-ARS or C8-ARS for an ARS with blank C8 emulsion).

2.2 Fabrication of ARSs

ARSs were polymerized within custom 48-well plates made by machining 9.5 mm diameter holes in a sheet of poly(methyl methacrylate) (85 mm × 125 mm × 5.5 mm). A Tegaderm membrane (3M HealthCare, St. Paul, MN USA) was adhered to the bottom of the sheet to create a well bottom. The wells were blocked with 10 mg/mL bovine serum albumin for at least 30 minutes to facilitate later removal of the ARSs.

A stock solution of bovine fibrinogen (Sigma-Aldrich) was prepared at 20 mg/mL clottable protein in Dulbecco's modified Eagle's media (DMEM). Bovine lung aprotinin (Sigma-Aldrich) was added at 0.1 U/mL and the solution was degassed in a vacuum chamber to

facilitate complete dissolution of the fibrinogen and to minimize the presence of bubbles. ARSs (total volume = 0.3 mL, diameter = 9.5 mm, height = 4.2 mm) were prepared by combining the fibrinogen solution, DMEM, bovine thrombin (Thrombin-JMI, Pfizer, NY, NY, USA), as well as emulsion and aliquoting the mixture into the well plate. The final concentrations of fibrinogen, aprotinin, thrombin, and emulsion were 10 mg/mL, 0.05 U/mL, 2 U/mL and 1% (v/v), respectively. For a subset of the *in vivo* experiments, the ARSs also contained 150 μg/mL Alexa Fluor 647 human fibrinogen conjugate (Molecular Probes, Eugene, OR, USA). The ARSs were allowed to polymerize for 15 minutes at room temperature. Following polymerization, the top of the plate was sealed with another Tegaderm membrane.

For an ARS where only half of the scaffold was exposed to US (i.e., +US upper, +US lower), the ARS was polymerized using a two-step, bi-layer approach. An ARS of one half volume (i.e., 0.15 mL) was polymerized, sealed within the plate, and exposed to US to generate ADV (methods described in the subsequent section). Following US exposure, another ARS of one half volume was overlaid and polymerized on top of the first layer.

2.3 Exposure of ARSs to US

US exposures were performed in a water tank (30 cm × 60 cm × 30 cm) filled with degassed (12–22% O_2 saturation), deionized water at 37°C. A calibrated, focused, single-element transducer (H108, 2.5 MHz, f-number = 0.83, focal length = 50 mm, Sonic Concepts, Inc., Bothell, WA USA) was used to generate ADV within the ARSs. The transducer was connected to a three-axis positioning system controlled by MATLAB (The MathWorks, Natick, MA, USA) and positioned beneath the plate containing the ARSs, which was submerged in the tank. The position of the axial focus of the transducer, with respect to the bottom of the plate, was determined via a pulse-echo technique using a pulser-receiver (5077PR, Olympus, Center Valley, PA, USA).

The transducer was driven by pulsed waveforms generated using a waveform generator (33500B, Agilent Technologies, Santa Clara, CA, USA) and amplified by a gated radiofrequency amplifier (GA-2500A Ritec Inc, Warwick, RI, USA). The amplified waveform was passed through a matching circuit (H108_3 MN, Sonic Concepts) to reduce the impedance mismatch between the transducer and amplifier. Waveforms were monitored with an oscilloscope (HDO4034, Teledyne LeCroy, Chestnut Ridge, NY, USA). To generate ADV within the ARSs, the following acoustic parameters were used: 8.0 MPa peak rarefactional pressure, 5.4 μs pulse duration, and 100 Hz pulse repetition frequency. We have previously demonstrated that this peak rarefactional pressure was suprathreshold for both ADV and inertial cavitation within the ARSs [21, 29]. During exposure, the transducer was laterally rastered across each ARS at a speed of 5 mm/s with a 0.5 mm spacing between raster lines. Exposures were done at three axial planes located 3 mm, 2 mm, and 1 mm above the well bottom, with exposures completed from the top/distal (i.e., 3 mm) to bottom/proximal (i.e., 1 mm) direction. The time required to complete the US exposure for each ARS was approximately 120 s.

2.4 *In vitro* release of bFGF

Following US exposure (i.e., day 0), a subset of the ARSs were imaged with an inverted microscope (Eclipse Ti-E, Nikon, Melville, NY, USA), monochromatic digital camera (Retiga R6, Teledyne, Tucson, AZ, USA) and MetaMorph software (Universal Imaging/ Molecular Devices Corporation, Union City, CA, USA). The remaining ARSs were aseptically transferred to 24-well culture plates (Fisher Scientific, Pittsburgh, PA, US) and overlaid with 1 mL of DMEM supplemented with 100 U/mL penicillin, 100 μg/mL streptomycin, and 2.5 μg/mL amphotericin B (Life Technologies). The plate was placed in a standard tissue culture incubator (37°C, 5% carbon dioxide) during the duration of the experiment. The overlying media was sampled daily by collecting 0.5 mL of the media for 7 days and replacing the collected volume with fresh media. The concentration of bFGF released into the media was measured using an enzyme-linked immunosorbent assay (ELISA) (DY233, R&D System, Inc., Minneapolis, MN, USA) according to the manufacturer's instructions. As done previously, bFGF release data were normalized by the maximum release from fibrin gels containing unencapsulated bFGF [21].

2.5 *In vivo* studies

This *in vivo* research was conducted with the approval of the Institutional Animal Care & Use Committee at the University of Michigan. Female SKH1-Elite mice (n = 37, 4–6 weeks old, 22.3 ± 2.6 g, Charles River Laboratories, Wilmington, MA, USA) were anesthetized with isoflurane (5% for induction and 1.5% for maintenance). The skin was disinfected with povidone-iodine (Betadine, Purdue Products, Stamford, CT, USA). Two full thickness skin incisions approximately 1 cm in length were made in the lower dorsal region parallel to and on either side of the spine. Small pouches were bluntly dissected in the subcutaneous tissue and one ARS was implanted in each pouch. The wounds were closed with interrupted silk sutures (6–0, Ethicon, New Brunswick, NJ, USA). Experimental groups for bFGF-loaded ARSs consisted of four different spatial patterns of ADV: −US, +US whole, +US upper, and +US lower. For +US whole, ADV was generated within the entire volume of the ARS. For +US upper and +US lower, ADV was generated in one layer of the bi-layer ARS (as described above); the layer with ADV was placed proximal to the skin and underlying muscle for +US upper and +US lower, respectively. Control groups received implants consisting of 10 mg/mL fibrin (only), 10 mg/mL fibrin with 1 μg bFGF, and ARSs with blank (i.e., without bFGF) emulsion.

The implanted ARSs were imaged on day 0 (i.e., day of implantation), 1, 3, and 7 using a ZS3 ultrasound system (Mindray, Mahwah, NJ, USA) and a prototype L25–8 linear probe operating at 25 MHz with an imaging depth of 2 cm. The acoustic output of the probe was set to minimum (i.e., mechanical index = 0.3) to prevent ADV. B-mode US images were acquired in a sagittal orientation at the thickest cross-section of the scaffold. Scaffold height and intensity (from displayed pixel values) were calculated in ImageJ (National Institutes of Health, Bethesda, MD, USA).

2.6 Histology and Morphometric Analyses

Mice were euthanized on day 7 post implantation. The implants were harvested with the surrounding tissue, bisected parallel to the skin incision, and fixed overnight in aqueous

buffered zinc formalin (Formalde-Fresh, Fisher Scientific, Waltham, MA USA). The tissue samples were transferred into 70% (v/v) ethanol until processing and embedding in paraffin at the University of Michigan Microscopy & Image Analysis Laboratory. Serial sections (thickness: 5 μm) were cut from the embedded tissue and transferred onto pre-cleaned glass slides (Fisherbrand Superfrost Plus, Thermo Fisher Scientific, Waltham, MA, USA) for histological analysis. Tissue sections were stained with hematoxylin and eosin (H&E) to visualize the overall tissue morphology. Tissue sections were immunohistochemically stained using a rabbit anti-mouse vimentin primary antibody (ab92547, Abcam, Cambridge, MA USA), rabbit anti-mouse Ki-67 primary antibody (ab15580, Abcam), rabbit anti-mouse CD31 primary antibody (ab124432, Abcam), and rabbit anti-mouse α-smooth muscle actin (SMA) primary antibody (ab32575, Abcam). A goat anti-rabbit secondary labeled polymer-horseradish peroxidase conjugate (Envision+ System-HRP (DAB), Dako North America, Inc., Carpinteria, CA USA) was used with all primary antibodies. Staining specificity was confirmed by staining with only the secondary conjugate.

Tissue sections were imaged with an inverted microscope, color digital camera (DS-Fi3, Nikon), and associated software (NIS-Elements, Nikon). Grayscale and fluorescence images were captured with a monochromatic digital camera. The following parameters were calculated from the acquired images: height of the scaffold, macroporosity of the implant, distance of cell migration, and thickness of the granulation tissue surrounding the implant. Macroporosity, which was calculated in ImageJ by thresholding the images, was defined as the ratio of the non-fibrin area divided by the total image area. A macroporosity of 0% indicated that the scaffold contained only fibrin. The distance of cell migration was determined by measuring the distance that host cells traversed the initially acellular implant from the ARS-host interface, whereby a distance of zero indicated no cell migration. The upper and lower thicknesses of granulation tissue were measured from the panniculus carnosus to the top of the ARS and bottom of the ARS to the underlying skeletal muscle, respectively. The density of blood vessels, defined as CD31+ structures possessing a lumen within the granulation tissue, was also determined. All morphometric analyses were done in a blinded manner by trained readers.

2.7 Statistics

Statistical analyses were performed using GraphPad Prism software (GraphPad Software, Inc., La Jolla, CA USA). All data are expressed as the mean ± standard error of the mean of measured quantities. For *in vitro* experiments, the rate constant (K) was determined by fitting the data to a first-order exponential approximation of solute diffusion in a high porous hydrogel [30]. For morphometric parameters derived from the histological images, measurements were averaged across five locations across the entire length of the scaffold and then averaged across multiple scaffolds. Significant differences between groups were determined using a one-way ANOVA followed by Tukey's multiple comparisons test. Significance levels and the number of independent replicates is listed within each figure caption.

2. Results

3.1 Characterization of emulsions

The mean diameters for the bFGF-C6, bFGF-C8, and C8 emulsions (n=3–5 per group) were 6.9 ± 0.1, 7.8 ± 0.3, and 6.2 ± 0.2 μm, respectively. There were significant differences between all groups. The coefficients of variation for the bFGF-C6, bFGF-C8, and C8 emulsions were 19.0 ± 1.6, 23.8 ± 4.9, and 19 ± 1.2%, respectively. There were no differences between groups.

3.2 *In vitro* bFGF release

bFGF release from the ARSs was measured for 7 days (Figure 1A,B). Starting one day after exposure, US caused significantly greater release from bFGF-C6-ARSs and bFGF-C8-ARSs compared to the corresponding −US controls. Significantly greater release, for both −US and +US whole conditions, was observed when comparing bFGF-C6-ARSs versus bFGF-C8-ARSs. The rate of release (K) in response to US was 6.8-fold greater for bFGF-C8-ARSs (i.e., 2.7 day^{-1}) compared to bFGF-C6-ARSs (i.e., 0.4 day^{-1}).

As can be seen in microscope images, distinct morphological differences were observed in the ARSs following US exposure (Figure 1C). Bubbles were seen in C6-ARSs whereas in C8-ARSs, no bubbles were observed. However, there were larger droplets within the C8-ARSs, as well as droplets that appeared irregularly-shaped (i.e., non-circular).

3.3 Longitudinal morphology of *in situ* ARSs

The subcutaneously-implanted ARSs were longitudinally imaged using B-mode US (Figure 2). The ARS was distinct from the overlying skin and underlying skeletal muscle. Compared to a hypoechoic scaffold containing only fibrin, the ARSs appeared echoic (Figure 2A), with bFGF-C6-ARS (+US whole) qualitatively displaying the greatest echogenicity and acoustic shadowing in distal regions. The echogenicities of the ARSs were quantified (Figure 2B). bFGF-C6-ARSs displayed significantly greater pixel intensity following US exposure compared to the −US controls across all timepoints. This elevated intensity remained relatively constant during the experiment. Conversely, the intensity of the −US group increased over time, with significant differences relative to day 0 beginning on day 3. With bFGF-C8-ARSs, there were no significant differences between −US and +US whole groups across any timepoints or differences relative to day 0.

The heights of the ARSs, taken at the thickest cross-section, are shown (Figure 2C). For the bFGF-C6-ARSs exposed to US, measurement of the scaffold height was facilitated based on anatomical features from the cutaneous and subcutaneous contours. A decrease in scaffold height was observed for bFGF-C6-ARS (−US) beginning on day 1, which was a similar trend as fibrin only scaffolds. Comparatively, scaffold height remained relatively constant for bFGF-C6-ARSs that were exposed to one of three patterns of US exposure. With bFGF-C8-ARSs, all scaffolds irrespective of US exposure displayed a significant reduction in height, with up to a 44% decrease on day 1.

3.4 Effect of the spatial pattern of ADV on ARS morphology

The ARSs and surrounding tissue were harvested 7 days after implantation and stained with H&E (Figure 3). Morphological features were also examined via fluorescence microscopy due to the inclusion of Alexa Fluor 647-labeled fibrinogen within the scaffold (Figure 4). The fibrin within the ARSs appeared homogenous for the −US condition for both bFGF-C6-ARS and bFGF-C8-ARS. Microscale voids within the ARS were due to the presence of the emulsion and were largely absent from fibrin only scaffolds in the absence of US. Upon exposure to US, dramatic morphological changes were observed in regions of the ARSs exposed to US. Qualitatively, large macropores – regions within the ARSs devoid of fibrin were observed in the bFGF-C6-ARSs. Similar macropores, though smaller in size, were seen in the bFGF-C8-ARSs and with fibrin only scaffolds.

The heights of the ARSs, which were measured from histology, are displayed (Figure 5A,B). A significant increase in height occurred for bFGF-C6-ARS (+US whole) compared to the −US condition. No changes in height were observed for the corresponding conditions for the bFGF-C8-ARSs. This was consistent with results obtained by B-mode imaging in Figure 2B. For +US lower and +US upper patterns, the height of each layer within the bFGF-C6-ARSs correlated with US exposure; an inverse correlation was observed for bFGF-C8-ARSs. A quantification of scaffold macroporosity is also shown (Figure 5C, D). For both bFGF-C6-ARSs and bFGF-C8-ARSs, regions of the scaffold exposed to US had greater macroporosity than corresponding −US regions. With bFGF-C6-ARSs, macroporosities of up to 6.3 ± 0.6% and 90.3 ± 1.5% were measured for −US and +US regions, respectively. Conversely, a maximum of 2.5 ± 0.7% and 6.8 ± 0.8% were observed for −US and +US regions, respectively, for bFGF-C8-ARSs

3.5 Effect of the spatial pattern of ADV on host interactions with ARSs

Migration of host cells into the ARS was denoted by the presence of hematoxylin-positive structures within the initially acellular scaffold. As observed qualitatively in Figure 3, limited cell migration was observed in all of the bFGF-C6-ARS conditions. However, with bFGF-C8-ARSs, cell migration was more evident and spatially correlated with the pattern of US exposure. The distance of cell migration was also quantified (Figure 5E,F). There were no differences in cell migration across any of the bFGF-C6-ARS conditions, with a maximum distance of 30 ± 8 μm. With bFGF-C8-ARSs, there was a correlation between migration distance and the layer of the scaffold exposed to US. For example, with the +US upper pattern, host cells migrated 38 ± 12 μm and 244 ± 14 μm into the lower and upper layers of the ARS, respectively. Similarly, for the +US lower pattern, host cells migrated 172 ± 23 μm and 46 ± 7 μm into the lower and upper layers of the ARS, respectively. Thus, the directionality of host cell migration was dependent on the spatial pattern of ADV within the ARS. Interestingly, for the +US whole pattern, greater migration was observed in the upper region (i.e., 210 ± 43 μm) versus the lower region (i.e., 80 ± 24 μm). Layers of vascularized, granulation tissue were seen above and below the implanted ARSs. However, there were no differences in the thickness of the granulation tissue for any of the groups (Figure 5G, H). Additionally, there were no differences in the microvessel density (Supplemental Figure 1).

To investigate the necessity of bFGF release on host cell migration, *in vivo* studies were conducted with fibrin only and C8-ARSs, with and without US exposure. Despite the increase in scaffold macroporosity following US exposure, cell migration distance was significantly lower in all groups without bFGF release (Figure 6). Thus, cell migration was linked with the release bFGF from the ARS. The identity of the cells that migrated into the ARSs was elucidated using immunohistochemical staining (Figure 7). Qualitatively, cells within the ARS stained positively for vimentin, Ki-67, and SMA – thereby indicating cells of mesodermal/mesenchymal origin (e.g., fibroblasts). Approximately 44% and 61% of cells were both vimentin+ and SMA+ in bFGF-C8-ARSs exposed to +US upper and +US lower patterns, respectively. Few cells in the ARS were positive for CD31, though blood vessels in the surrounding granulation tissue were CD31+.

3. Discussion

In this study, the PFC species within the emulsion had a significant impact on the *in vitro* and *in vivo* properties of the ARSs, which ultimately impacted the *in vivo* host response. As seen with microscopy and B-mode imaging, exposure to suprathreshold US generated stable gas bubbles in bFGF-C6-ARSs. In general, bubbles were larger than 20 μm in diameter, which is the approximate size predicted based on the initial droplet diameter and expansion based on the ideal gas law [9]. Thus significant coalescence and in-gassing occurred. Bubble formation lead to slower release kinetics of bFGF compared to bFGF-C8-ARSs, which did not contain bubbles. Micron-sized, phase-shift emulsions with C6 have been shown to form stable bubbles following ADV when suspended in both liquids [31] and hydrogels like polyacrylamide [32] or fibrin [33]. Consistent with our previous study [29], the bubbles generated in bFGF-C6-ARSs were a barrier for diffusion of the released payload, thus effectively increasing the path length of diffusion for bFGF.

ARSs were exposed to acoustic pulses at 8.0 MPa peak rarefactional pressure, which was far above the ADV threshold for ARSs with C8 emulsion (i.e., 2.6 ± 0.2 MPa [29]) and inertial cavitation (i.e., 3.9 ± 0.2 MPa [21]) threshold at 2.5 MHz. Due to the standing wave formation within the ARS, since the ARS was backed with air, higher pressures were present within the top 1 mm of the ARS [21]. Despite these elevated pressures, the likelihood for ADV to generate stable bubbles decreases if the bulk boiling point of the PFC exceeds the ambient temperature [34]. Given the difference between bulk boiling points of C6 (i.e., 56°C) and C8 (i.e., 100°C), stable gas bubble with the latter species was thermodynamically unfavorable. Vaporization followed by recondensation has been observed in prior experiments with phase-shift emulsions [35, 36]. With bFGF-C8-ARSs, microscopy showed evidence of emulsion vaporization followed by recondensation and coalescence, with the latter phenomenon facilitated by the close spacing of droplets. The lower release efficiency from bFGF-C8-ARSs following suprathreshold US could be attributed to droplet recondensation. Thus, stable gas bubble formation in response to ADV may assist in expelling the payload from the double emulsion.

Gas bubbles within bFGF-C6-ARSs remained present *in vivo* during the duration of the experiment, which inhibited the compaction of the ARS. Note that heights measured by B-mode US were larger than those measured from histology, which was attributed to the

volumetric loss experienced by tissue during fixation [37]. All bFGF-C8-ARS conditions and bFGF-C6-ARS (−US), which lacked bubbles, exhibited significant compaction within one day of subcutaneous implantation. Comparatively, scaffold compaction was not observed in a prior *in vitro* study [29]. Protein-based hydrogels, like fibrin, that are loaded with cells are known to compact based on cell-mediated remodeling of the hydrogel [38]. However, the ARSs in this study were all initially acellular, and thus other mechanisms were involved at this early timepoint – potentially compression of the ARS by the overlying skin as well as osmotic equilibration in the subcutaneous space. Additionally, compaction has been shown to correlate inversely with hydrogel stiffness [39]. Thus, since ARSs become significantly stiffer following ADV and stable gas bubble formation [10], this could partially explain the observed results. On day 7, cell-mediated compaction correlated with the region of the ARS exposed to US for bFGF-C8-ARS (+US lower) and bFGF-C8-ARS (+US upper). Therefore, cell mediated compaction and host cell migration were linked. Compaction of the ARS could also slow the rate of bFGF release since a prior study demonstrated an inverse correlation between fibrin concentration and the rate of bFGF release [40].

Unlike bFGF-C6-ARS - where stable gas bubbles generated by US remained trapped within the fibrin matrix - the combined effects of vaporization, recondensation, and coalescence generated macropores within the bFGF-C8-ARS. Inertial cavitation also generated macropores in fibrin-only scaffolds. Other groups have used the mechanical effects generated by ultrasound-responsive particles to alter the structure of scaffolds. For example, ADV and subsequent inertial cavitation of micron-sized, phase-shift emulsions was shown to cause erosion in agarose-based, vessel phantoms [41]. Microporous poly(lactic-co-glycolic acid) scaffolds were generated via the incorporation of microbubbles followed by phase separation and lyophilization [42]. Additionally, micropores were created in agarose scaffolds by incorporating microbubbles, followed by the application of hydrostatic pressure [43]. The generation of open, interconnected micro-sized pores within hydrogels, which often intrinsically possess submicron-sized pores, has been used to facilitate drug delivery and to enhance regenerative events such as vascularization [44, 45]. In this study, generation of macropores in the absence of bFGF release was not sufficient to enhance cell migration.

Cell migration is a critical process within wound healing and tissue regeneration. In bFGF-C6-ARSs, stable bubbles inhibited host cell migration into the scaffold. With bi-layer bFGF-C8-ARSs, cell migration correlated with the region of the ARS exposed to US. Two hypotheses could explain why greater cell migration was observed in the upper versus lower regions for the +US whole pattern. First, each ARS was implanted in a pouch made in the subcutaneous tissue following a full thickness skin incision. This procedure disrupted the epidermis and dermis more significantly than the hypodermis and underlying muscle layers. Second, the fascia overlying the muscle layer provided a barrier to cell migration, which would lead to faster cell migration in the upper region. Based on immumohistochemical staining of ARSs on day 7, cells within the ARS were likely proliferating fibroblasts (vimentin+, Ki-67+) and myofibroblasts (vimentin+, Ki-67+, SMA+), in addition to the surrounding granulation tissue that contained blood vessels (CD31+). This was consistent with the cutaneous wound healing response where different GFs stimulate fibroblast proliferation, migration, as well as differentiation into a myofibroblast phenotype [46]. For example, bFGF is known to stimulate proliferation of fibroblasts [47].

A limitation of the current study is that the US was applied to *ex situ* ARSs. This was done to produce precisely patterned regions of US exposure within the bi-layer scaffolds. Therefore, the impact of *in situ* US on implanted ARSs was not elucidated in the SKH1-Elite mouse model. Previously, we applied *in situ* US to subcutaneously-implanted ARSs in BALB/c mice to demonstrate the impact of temporally-controlled bFGF release on angiogenesis [19]. As has been done with other US-based therapies [48, 49], image guidance would facilitate the study of spatial control using *in situ* US. Anatomical features of the ARS and surrounding tissue could be mapped and registered with the focus of the therapeutic US transducer. Furthermore, the literature confirms that mice display differences across strains in terms of wound healing and angiogenesis [50], and this motivates future studies investigating the impact of spatially-patterned, *in situ* US. Additionally, in a mouse model, the effect of acoustic attenuation on US propagation is minimal. For translational studies, the transmitted acoustic pressures will need to account for attenuation, which is dependent on the implantation depth of the ARS and the types of tissue overlying the ARS. Future studies will also investigate the immune response elicited by the ARS and *in situ* US exposure, which has been shown in other US-based therapies to induce a localized immune response [51].

4. Conclusions

We have demonstrated that suprathreshold US can be used to spatiotemporally-control biological processes within ARSs via the localized release of bFGF. Suprathreshold US generated stable bubbles in bFGF-C6-ARSs as well as transiently-stable bubbles in bFGF-C8-ARSs. Stable bubbles inhibited the rate of bFGF release, compaction of the ARS, and host cell migration into the ARS. In bFGF-C8-ARSs, exposure to suprathreshold US correlated with the generation of macropores within the fibrin matrix, migration of host cells into the ARS, and cell-mediated compaction. Based on immunohistochemistry, host cells within the matrix were likely fibroblasts and myofibroblasts. Control studies confirmed that increased host cell migration into the ARS was dependent on bFGF release. Among ARS groups, no differences were observed with the thickness of the granulation surrounding the scaffold or density of microvessels in the granulation tissue. These results show that spatially patterning suprathreshold US within bFGF-C8-ARSs can be used to elucidate a spatially patterned response from the host. Future studies will investigate how these findings can be applied to spatially pattern other regenerative processes.

Supplementary Material

Refer to Web version on PubMed Central for supplementary material.

Acknowledgments

This work was supported by NIH Grant R01HL139656 (M.L.F.). H.J. was supported by funds from the Second Affiliated Hospital of South China University of Technology. L.H. was supported by funds from the National Key R&D Program of China 2017YFC0107300. Special thanks to Dr. Allen Brooks (Department of Radiology) for assisting with the synthesis of the fluorosurfactant and Dr. William Weadock (Department of Radiology) for assisting with 3D printing of materials related to the US exposure setup. Additionally, we thank Zhewen Deng, Yanbo Feng, and Karsyn Kazyak for assistance with histology and Alexander Hostetler with *in vitro* imaging.

References

[1]. Jeon O, Kang SW, Lim HW, Chung JH, Kim BS, Long-term and zero-order release of basic fibroblast growth factor from heparin-conjugated poly(L-lactide-co-glycolide) nanospheres and fibrin gel, Biomaterials 27(8) (2006) 1598–1607. [PubMed: 16146647]

[2]. Zhao W, Han Q, Lin H, Sun W, Gao Y, Zhao Y, Wang B, Wang X, Chen B, Xiao Z, Dai J, Human basic fibroblast growth factor fused with Kringle4 peptide binds to a fibrin scaffold and enhances angiogenesis, Tissue engineering. Part A 15(5) (2009) 991–8. [PubMed: 18771415]

[3]. Richardson TP, Peters MC, Ennett AB, Mooney DJ, Polymeric system for dual growth factor delivery, Nat Biotechnol 19(11) (2001) 1029–34. [PubMed: 11689847]

[4]. Trappmann B, Baker BM, Polacheck WJ, Choi CK, Burdick JA, Chen CS, Matrix degradability controls multicellularity of 3D cell migration, Nat Commun 8(1) (2017) 371. [PubMed: 28851858]

[5]. Chen RR, Silva EA, Yuen WW, Mooney DJ, Spatio-temporal VEGF and PDGF delivery patterns blood vessel formation and maturation, Pharmaceutical research 24(2) (2007) 258–64. [PubMed: 17191092]

[6]. Wade RJ, Bassin EJ, Gramlich WM, Burdick JA, Nanofibrous hydrogels with spatially patterned biochemical signals to control cell behavior, Adv Mater 27(8) (2015) 1356–62. [PubMed: 25640972]

[7]. Jeon O, Lee K, Alsberg E, Spatial Micropatterning of Growth Factors in 3D Hydrogels for Location-Specific Regulation of Cellular Behaviors, Small 14(25) (2018) e1800579. [PubMed: 29782703]

[8]. Ahlfeld T, Akkineni AR, Forster Y, Kohler T, Knaack S, Gelinsky M, Lode A, Design and Fabrication of Complex Scaffolds for Bone Defect Healing: Combined 3D Plotting of a Calcium Phosphate Cement and a Growth Factor-Loaded Hydrogel, Annals of biomedical engineering 45(1) (2017) 224–236. [PubMed: 27384939]

[9]. Kripfgans OD, Fowlkes JB, Miller DL, Eldevik OP, Carson PL, Acoustic droplet vaporization for therapeutic and diagnostic applications, Ultrasound Med Biol 26(7) (2000) 1177–1189. [PubMed: 11053753]

[10]. Fabiilli ML, Wilson CG, Padilla F, Martin-Saavedra FM, Fowlkes JB, Franceschi RT, Acoustic droplet-hydrogel composites for spatial and temporal control of growth factor delivery and scaffold stiffness, Acta Biomater 9(7) (2013) 7399–409. [PubMed: 23535233]

[11]. Moncion A, Arlotta KJ, Kripfgans OD, Fowlkes JB, Carson PL, Putnam AJ, Franceschi RT, Fabiilli ML, Design and Characterization of Fibrin-Based Acoustically Responsive Scaffolds for Tissue Engineering Applications, Ultrasound Med Biol 42(1) (2016) 257–71. [PubMed: 26526782]

[12]. Li DS, Kripfgans OD, Fabiilli ML, Fowlkes JB, Bull JL, Initial nucleation site formation due to acoustic droplet vaporization, Applied physics letters 104(6) (2014).

[13]. Shpak O, Verweij M, Vos HJ, de Jong N, Lohse D, Versluis M, Acoustic droplet vaporization is initiated by superharmonic focusing, Proceedings of the National Academy of Sciences of the United States of America 111(5) (2014) 1697–702. [PubMed: 24449879]

[14]. Kripfgans OD, Zhang M, Fabiilli ML, Carson PL, Padilla F, Swanson SD, Mougenot C, Fowlkes JB, Mougenot C, Acceleration of ultrasound thermal therapy by patterned acoustic droplet vaporization, The Journal of the Acoustical Society of America 135(1) (2014) 537–44. [PubMed: 24437794]

[15]. Vernon RB, Sage EH, A novel, quantitative model for study of endothelial cell migration and sprout formation within three-dimensional collagen matrices, Microvasc Res 57(2) (1999) 118–133. [PubMed: 10049660]

[16]. Chabut D, Fischer AM, Colliec-Jouault S, Laurendeau I, Matou S, Le Bonniec B, Helley D, Low molecular weight fucoidan and heparin enhance the basic fibroblast growth factor-induced tube formation of endothelial cells through heparan sulfate-dependent alpha6 overexpression, Mol Pharmacol 64(3) (2003) 696–702. [PubMed: 12920206]

[17]. de la Puente P, Ludena D, Fernandez A, Aranda JL, Varela G, Iglesias J, Autologous fibrin scaffolds cultured dermal fibroblasts and enriched with encapsulated bFGF for tissue engineering, J. Biomed. Mater. Res. Part A 99a(4) (2011) 648–654.

[18]. Dong X, Lu X, Kingston K, Brewer E, Juliar BA, Kripfgans OD, Fowlkes JB, Franceschi RT, Putnam AJ, Liu Z, Fabiilli ML, Controlled delivery of basic fibroblast growth factor (bFGF) using acoustic droplet vaporization stimulates endothelial network formation, Acta Biomater 97 (2019) 409–419. [PubMed: 31404713]

[19]. Moncion A, Lin M, O'Neill EG, Franceschi RT, Kripfgans OD, Putnam AJ, Fabiilli ML, Controlled release of basic fibroblast growth factor for angiogenesis using acoustically-responsive scaffolds, Biomaterials 140 (2017) 26–36. [PubMed: 28624705]

[20]. Moncion A, Lin M, Kripfgans OD, Franceschi RT, Putnam AJ, Fabiilli ML, Sequential payload release from acoustically-responsive scaffolds uinsg focused ultrasound, Ultrasound Med Biol 44(11) (2018) 2323–2335. [PubMed: 30077413]

[21]. Aliabouzar M, Jivani A, Lu X, Kripfgans OD, Fowlkes JB, Fabiilli ML, Standing wave-assisted acoustic droplet vaporization for single and dual payload release in acoustically-responsive scaffolds, Ultrasonics sonochemistry in press (2020).

[22]. Lamalice L, Le Boeuf F, Huot J, Endothelial cell migration during angiogenesis, Circulation research 100(6) (2007) 782–94. [PubMed: 17395884]

[23]. Nevius E, Gomes AC, Pereira JP, Inflammatory Cell Migration in Rheumatoid Arthritis: A Comprehensive Review, Clin Rev Allergy Immunol 51(1) (2016) 59–78. [PubMed: 26511861]

[24]. Sakar MS, Eyckmans J, Pieters R, Eberli D, Nelson BJ, Chen CS, Cellular forces and matrix assembly coordinate fibrous tissue repair, Nat Commun 7 (2016) 11036. [PubMed: 26980715]

[25]. Miller ED, Li K, Kanade T, Weiss LE, Walker LM, Campbell PG, Spatially directed guidance of stem cell population migration by immobilized patterns of growth factors, Biomaterials 32(11) (2011) 2775–85. [PubMed: 21272933]

[26]. Han L, Mao Z, Wu J, Guo Y, Ren T, Gao C, Directional cell migration through cell-cell interaction on polyelectrolyte multilayers with swelling gradients, Biomaterials 34(4) (2013) 975–84. [PubMed: 23127331]

[27]. Lo AH, Kripfgans OD, Carson PL, Fowlkes JB, Spatial Control of Gas Bubbles and Their Effects on Acoustic Fields, Ultrasound Med Biol 32(1) (2006) 95–106. [PubMed: 16364801]

[28]. Bezagu M, Errico C, Chaulot-Talmon V, Monti F, Tanter M, Tabeling P, Cossy J, Arseniyadis S, Couture O, High spatiotemporal control of spontaneous reactions using ultrasound-triggered composite droplets, J Am Chem Soc 136(20) (2014) 7205–8. [PubMed: 24785681]

[29]. Lu X, Dong X, Natla S, Kripfgans OD, Fowlkes JB, Wang X, Franceschi R, Putnam AJ, Fabiilli ML, Parametric Study of Acoustic Droplet Vaporization Thresholds and Payload Release From Acoustically-Responsive Scaffolds, Ultrasound Med Biol 45(9) (2019) 2471–2484. [PubMed: 31235205]

[30]. Patil NS, Dordick JS, Rethwisch DG, Macroporous poly(sucrose acrylate) hydrogel for controlled release of macromolecules, Biomaterials 17(24) (1996) 2343–2350. [PubMed: 8982474]

[31]. Couture O, Faivre M, Pannacci N, Babataheri A, Servois V, Tabeling P, Tanter M, Ultrasound internal tattooing, Med Phys 38(2) (2011) 1116–23. [PubMed: 21452748]

[32]. Duncanson WJ, Arriaga LR, Ung WL, Kopechek JA, Porter TM, Weitz DA, Microfluidic Fabrication of Perfluorohexane-Shelled Double Emulsions for Controlled Loading and Acoustic-Triggered Release of Hydrophilic Agents, Langmuir 30(46) (2014) 13765–13770. [PubMed: 25340527]

[33]. Moncion A, Arlotta KJ, O'Neill EG, Lin M, Mohr LA, Franceschi RT, Kripfgans OD, Putnam AJ, Fabiilli ML, In vitro and in vivo assessment of controlled release and degradation of acoustically-responsive scaffolds, Acta Biomater 46 (2016) 221–33. [PubMed: 27686040]

[34]. Fabiilli ML, Haworth KJ, Fakhri NH, Kripfgans OD, Carson PL, Fowlkes JB, The Role of Inertial Cavitation in Acoustic Droplet Vaporization, IEEE Transactions on Ultrasonics, Ferroelectrics, and Frequency Control 56(5) (2009) 1006–1017.

[35]. Reznik N, Shpak O, Gelderblom EC, Williams R, de Jong N, Versluis M, Burns PN, The efficiency and stability of bubble formation by acoustic vaporization of submicron perfluorocarbon droplets, Ultrasonics 53(7) (2013) 1368–1376. [PubMed: 23652262]

[36]. Yu J, Chen XC, Villanueva FS, Kim K, Vaporization and recondensation dynamics of indocyanine green-loaded perfluoropentane droplets irradiated by a short pulse laser, Applied physics letters 109(24) (2016).

[37]. Chatterjee S, Artefacts in histopathology, J Oral Maxillofac Pathol 18(Suppl 1) (2014) S111–6. [PubMed: 25364159]

[38]. Jansen KA, Bacabac RG, Piechocka IK, Koenderink GH, Cells actively stiffen fibrin networks by generating contractile stress, Biophys J 105(10) (2013) 2240–51. [PubMed: 24268136]

[39]. Rowe SL, Lee S, Stegemann JP, Influence of thrombin concentration on the mechanical and morphological properties of cell-seeded fibrin hydrogels, Acta Biomater 3(1) (2007) 59–67. [PubMed: 17085089]

[40]. Jeon O, Ryu SH, Chung JH, Kim BS, Control of basic fibroblast growth factor release from fibrin gel with heparin and concentrations of fibrinogen and thrombin, Journal of Controlled Release 105(3) (2005) 249–259. [PubMed: 16088988]

[41]. Kang ST, Lin YC, Yeh CK, Mechanical bioeffects of acoustic droplet vaporization in vessel-mimicking phantoms, Ultrasonics sonochemistry 21(5) (2014) 1866–74. [PubMed: 24690297]

[42]. Nair A, Thevenot P, Dey J, Shen J, Sun MW, Yang J, Tang L, Novel polymeric scaffolds using protein microbubbles as porogen and growth factor carriers, Tissue engineering. Part C, Methods 16(1) (2010) 23–32. [PubMed: 19327002]

[43]. Lima EG, Durney KM, Sirsi SR, Nover AB, Ateshian GA, Borden MA, Hung CT, Microbubbles as biocompatible porogens for hydrogel scaffolds, Acta Biomater 8(12) (2012) 4334–4341. [PubMed: 22868194]

[44]. Fu J, Fan C, Lai WS, Wang D, Enhancing vascularization of a gelatin-based micro-cavitary hydrogel by increasing the density of the micro-cavities, Biomed Mater 11(5) (2016) 055012. [PubMed: 27716648]

[45]. Griffin DR, Weaver WM, Scumpia PO, Di Carlo D, Segura T, Accelerated wound healing by injectable microporous gel scaffolds assembled from annealed building blocks, Nature materials 14(7) (2015) 737–44. [PubMed: 26030305]

[46]. Singer AJ, Clark RA, Cutaneous wound healing, N Engl J Med 341(10) (1999) 738–46. [PubMed: 10471461]

[47]. Makino T, Jinnin M, Muchemwa FC, Fukushima S, Kogushi-Nishi H, Moriya C, Igata T, Fujisawa A, Johno T, Ihn H, Basic fibroblast growth factor stimulates the proliferation of human dermal fibroblasts via the ERK1/2 and JNK pathways, Br J Dermatol 162(4) (2010) 717–23. [PubMed: 19995368]

[48]. Ebbini ES, ter Haar G, Ultrasound-guided therapeutic focused ultrasound: current status and future directions, International journal of hyperthermia : the official journal of European Society for Hyperthermic Oncology, North American Hyperthermia Group 31(2) (2015) 77–89.

[49]. Schlesinger D, Benedict S, Diederich C, Gedroyc W, Klibanov A, Larner J, MR-guided focused ultrasound surgery, present and future, Med Phys 40(8) (2013).

[50]. Helisch A, Wagner S, Khan N, Drinane M, Wolfram S, Heil M, Ziegelhoeffer T, Brandt U, Pearlman JD, Swartz HM, Schaper W, Impact of mouse strain differences in innate hindlimb collateral vasculature, Arterioscl Throm Vas 26(3) (2006) 520–526.

[51]. Burks SR, Ziadloo A, Hancock HA, Chaudhry A, Dean DD, Lewis BK, Frenkel V, Frank JA, Investigation of cellular and molecular responses to pulsed focused ultrasound in a mouse model, PloS one 6(9) (2011) e24730. [PubMed: 21931834]

Statement of Significance

Hydrogels are commonly used in regenerative medicine for the delivery of growth factors (GFs). The spatial and temporal presentations of GFs are critical for directing regenerative processes, yet conventional hydrogels do not enable such control. We have developed a composite hydrogel, termed an acoustically-responsive scaffold (ARS), where GF release is non-invasively and spatiotemporally-controlled using focused ultrasound. The ARS consists of a fibrin matrix doped with a phase-shift emulsion loaded with GF, which is released when the ARS is exposed to ultrasound. In this *in vivo* study, we demonstrate that spatially patterning ultrasound within an ARS containing basic fibroblast growth factor (bFGF) can elicit a spatially-directed response from the host. Overall, these findings can be used in developing strategies to spatially pattern regenerative processes.

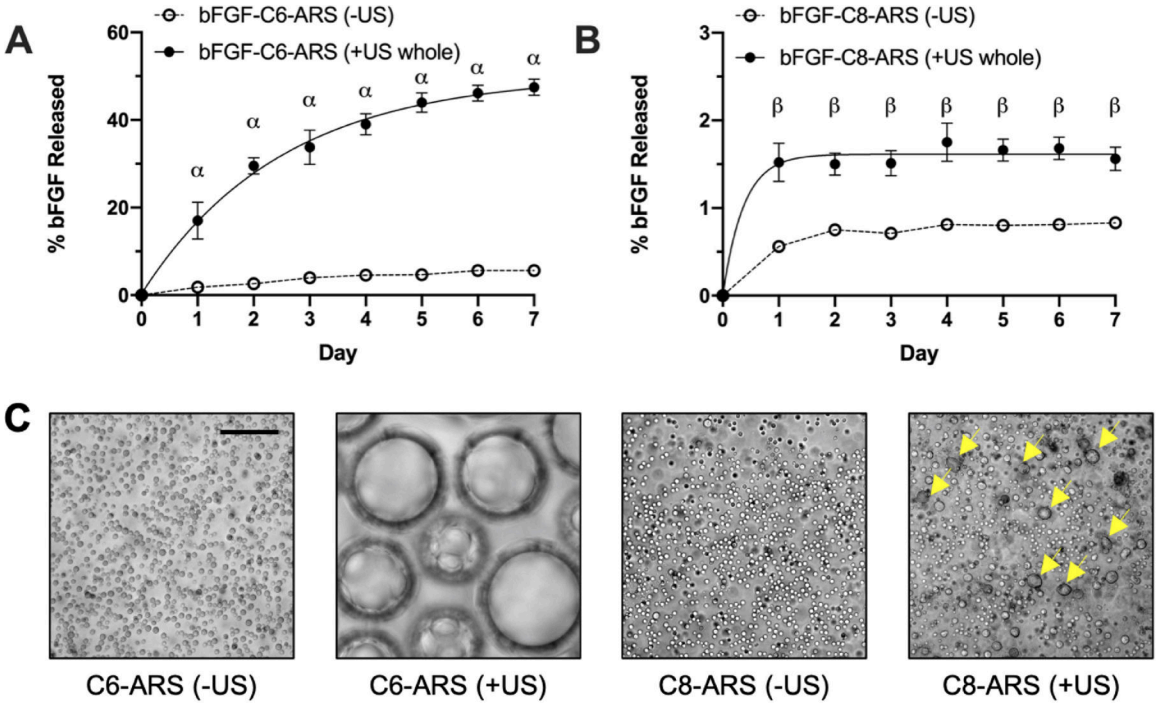

Figure 1.

In vitro release of bFGF from the acoustically-responsive scaffolds (ARSs) was dependent on the perfluorocarbon (PFC) species within the phase-shift emulsion. ARSs containing 1% (v/v) bFGF-loaded emulsion, with either (A) perfluorohexane (C6) or (B) perfluorooctane (C8), were polymerized and exposed to 2.5 MHz US on day 0. Data are represented as mean ± standard error of the mean (N=5 per condition). Statistically significant differences are denoted as follows: α: vs. bFGF-C6-ARS (−US) ($p < 0.001$) and β: vs. bFGF-C8-ARS (−US) ($p < 0.01$). C) Images of ARSs with either C6 or C8 emulsions show differences following US exposure. The images were taken within 1 hr following exposure. The yellow arrows denote droplets that appear to have coalesced. Scale bar for all images: 50 μm.

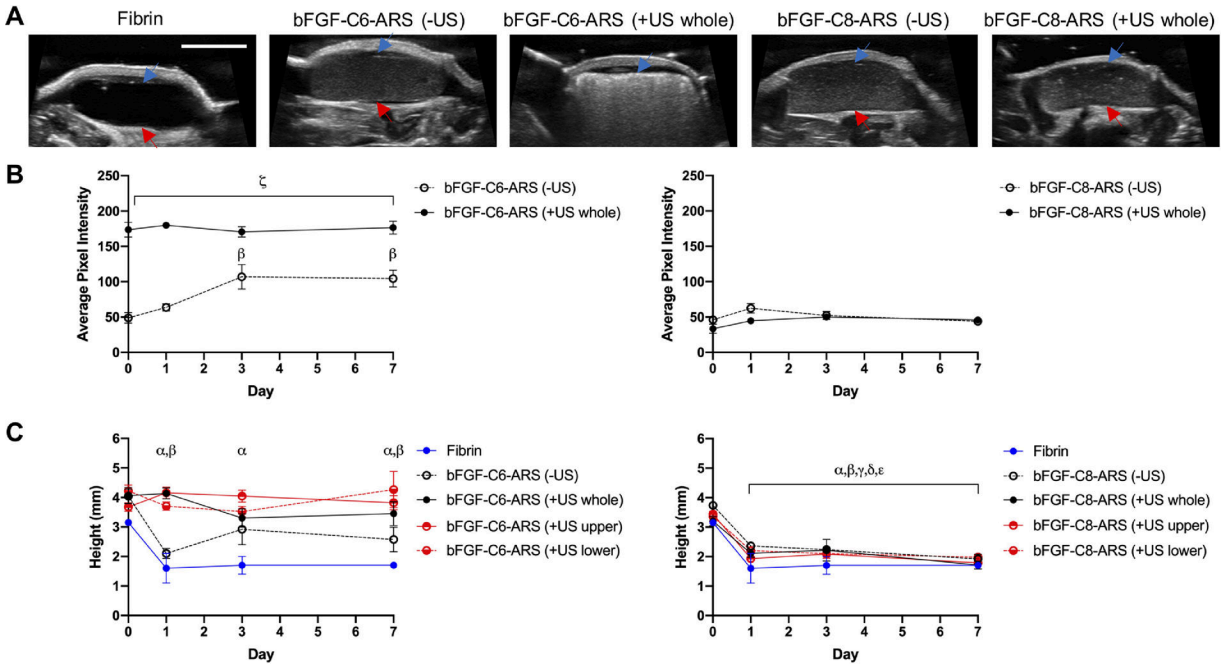

Figure 2.

ARSs were polymerized and exposed *ex situ* to US to generate acoustic droplet vaporization (ADV). The ARSs were implanted subcutaneously and longitudinally monitored *in vivo* using B-mode US. A) Transverse, B-mode images at 25 MHz show the *in situ* morphologies of the subcutaneously-implanted scaffolds on day 0. The blue arrow denotes the top interface of the ARS which was proximal to the overlying skin. The red arrow denotes the bottom interface of the ARS which was proximal to the underlying skeletal muscle. Scale bar for all images: 5 mm. The echogenicities (B) and heights (C) of ARSs containing bFGF-C6-emulsion (left) and bFGF-C8-emulsion (right) are displayed. Data are represented as mean ± standard error of the mean (N=5 per condition). Statistically significant differences ($p < 0.05$) are denoted as follows: α: vs. fibrin (day 0), β: vs. ARS (−US) (day 0), γ: vs ARS (+US whole) (day 0), δ: vs ARS (+US upper) (day 0), ε: vs ARS (+US lower) (day 0), and ζ vs. vs bFGF-C6-ARS (−US).

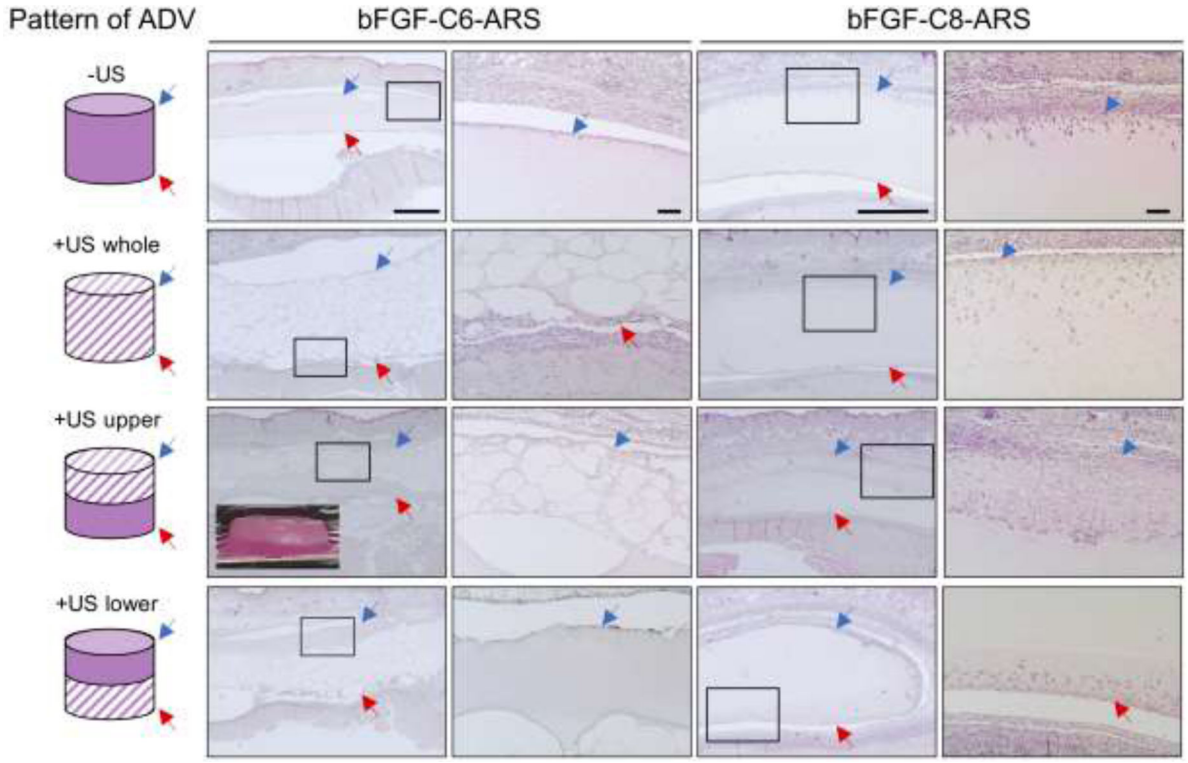

Figure 3.

ARSs with either bFGF-C6 or bFGF-C8 emulsion were polymerized and exposed *ex situ* to one of four different spatial patterns of 2.5 MHz US (far left column) prior to *in vivo* implantation on day 0. After 7 days, the ARSs and surrounding tissues were retrieved and stained with H&E, which enabled visualization of scaffold morphology and host cell migration. The blue arrow denotes the top interface of the ARS which was proximal to the overlying skin. The red arrow denotes the bottom interface of the ARS which was proximal to the underlying skeletal muscle. The second and fourth columns of images show zoomed-in panels from the first and third columns, respectively. Scale bars: 1 mm (columns 1 and 3) and 100 μm (columns 2 and 4). Inset: Image of an ARS exposed to the +US upper pattern. The height and diameter of the ARS is 4.2 mm and 9.5 mm, respectively.

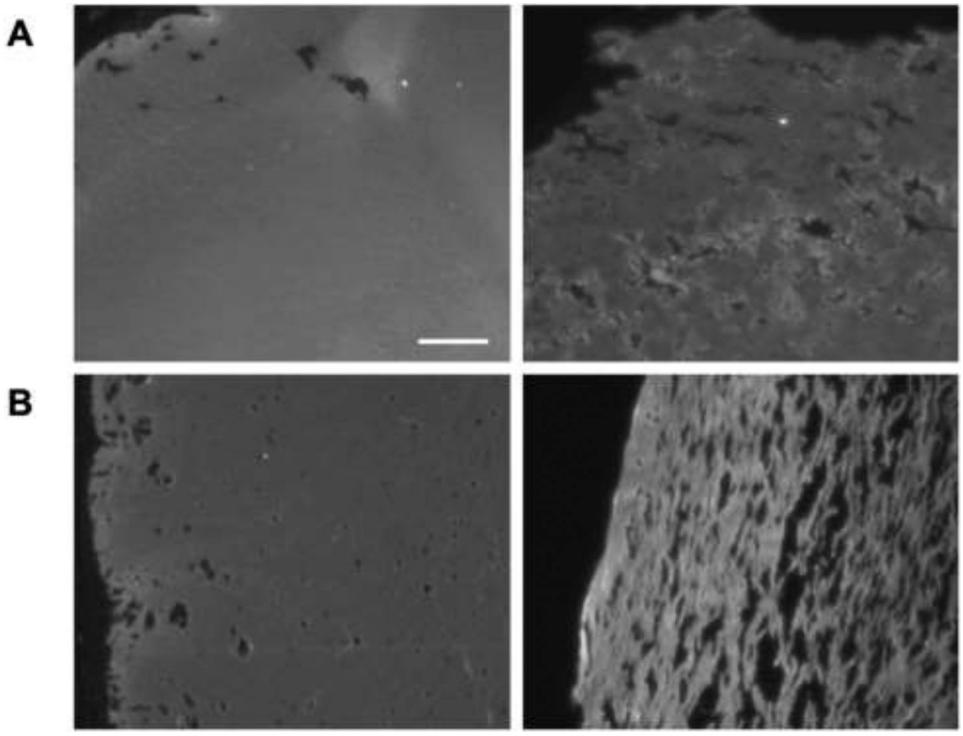

Figure 4.

Fluorescence images of A) fibrin (only) scaffolds and B) C8-ARSs highlight the increase in macroporosity with US exposure (right column) compared to −US condition (left column). Scaffolds, which contained Alexa Fluor 647-labeled fibrinogen, were polymerized and exposed to US *ex situ* prior to subcutaneous implantation. After 7 days, the scaffolds and surrounding tissue were harvested. Scale bar for all images: 100 μm

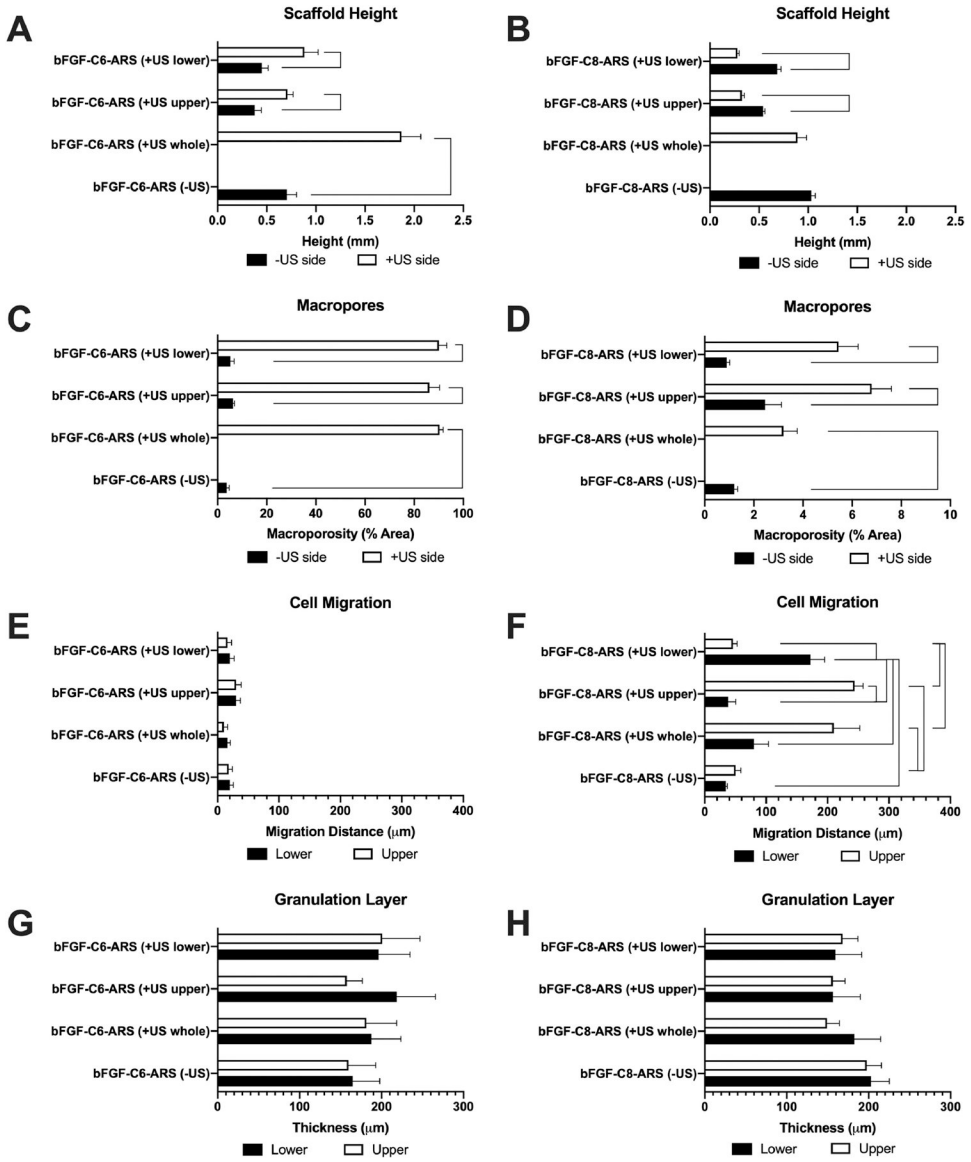

Figure 5.

After 7 days, the subcutaneously implanted ARSs and surrounding tissues were explanted and stained with H&E. The H&E images were quantitatively analyzed to determine (A,B) scaffold height, (C,D) the percent of macropores in the scaffold, (E,F) the distance of host cell migration into the scaffold, and (G,H) the thickness of the granulation tissue surrounding the scaffold. In panels A-D, the data are grouped according to US exposure. In panels E-H, the data are grouped based on the lower and upper regions of the ARS. Data are represented as mean ± standard error of the mean (N=5 per condition). Statistically significant differences ($p < 0.01$) are denoted.

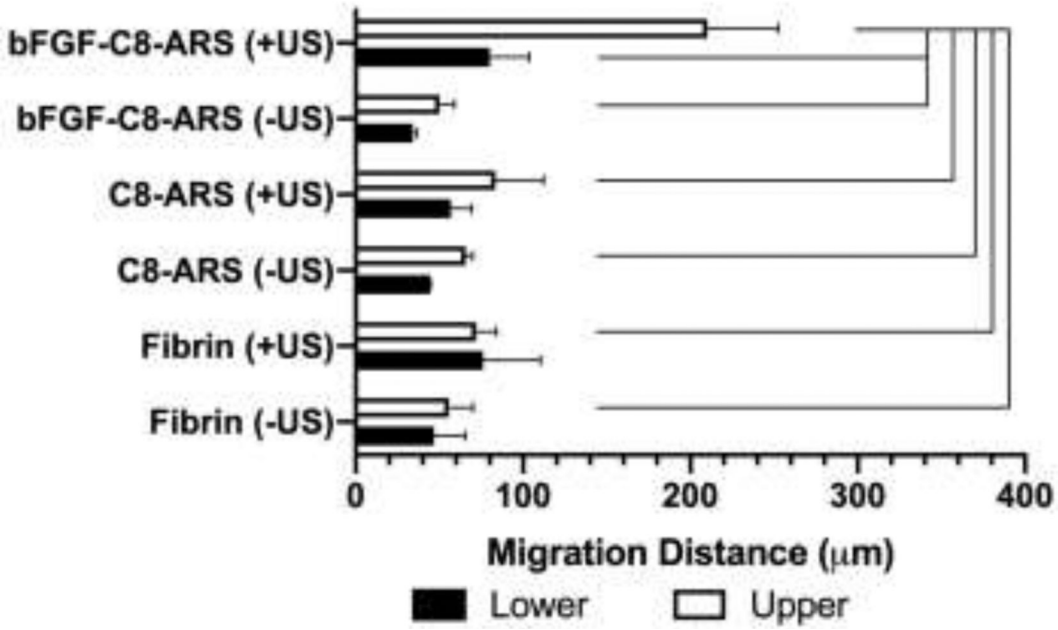

Figure 6.

Cell migration into the scaffold correlated with the US-triggered release of bFGF. In control experiments, fibrin only scaffolds or ARSs without bFGF (i.e., C8-ARS) were implanted subcutaneously implanted and harvested after 7 days. Prior to implantation, a subset of the scaffolds were exposed to 2.5 MHz US using the whole exposure pattern. The migration distance of host cells into the scaffolds was determined by quantifying the H&E images. Data are represented as mean ± standard error of the mean (N=3–5 per condition). Statistically significant differences ($p < 0.05$) are denoted.

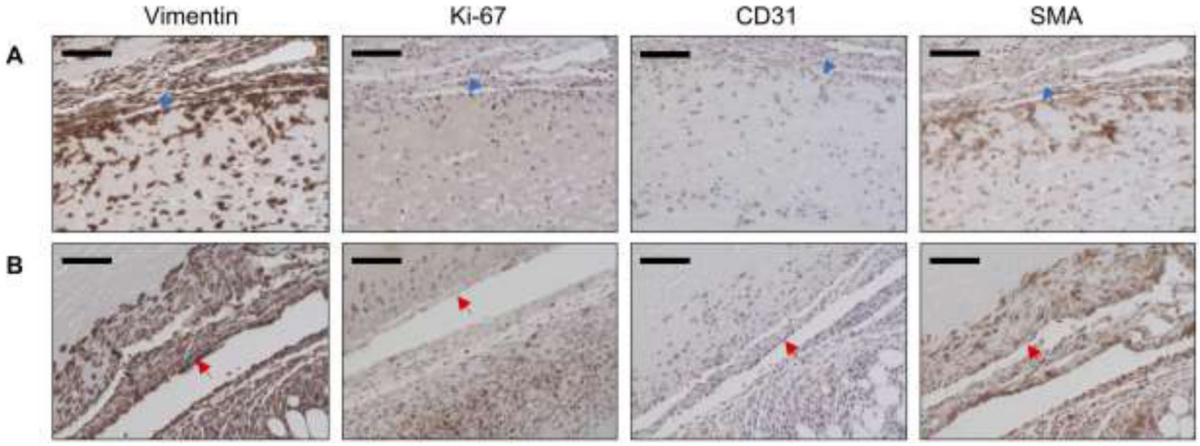

Figure 7.

Explanted ARSs were immunohistochemically stained for vimentin, Ki-67, CD31, and SMA. Panels A and B show upper and lower regions of bFGF-C8-ARSs exposed to the +US upper and +US lower patterns, respectively. The blue arrow denotes the top interface of the ARS which was proximal to the overlying skin. The red arrow denotes the bottom interface of the ARS which was proximal to the underlying skeletal muscle. Sections were counterstained with hematoxylin. Scale bar for all images: 100 μm.